Environ. Sci. Technol. **2007**, *41,* 6418−6424

Optimization of Nano- and Microiron Transport through Sand Columns Using Polyelectrolyte Mixtures

BIANCA W. HYDUTSKY, ELIZABETH J. MACK, BENJAMIN B. BECKERMAN, JOANNA M. SKLUZACEK, AND THOMAS E. MALLOUK*

Department of Chemistry, The Pennsylvania State University, University Park, Pennsylvania 16802

Sand-packed columns were used to study the transport of micro- and nanoiron particle suspensions modified with anionic polyelectrolytes. With microscale carbonyl iron powder (CIP), the profiles of initial and eluted particle diameters were compared with simulations based on classical filtration theory (CFT), using both the Tufenkji−Elimelech (TE) and Rajagopalan−Tien (RT) models. With particle size distributions that peaked in the submicron range, there was reasonable agreement between both models and the eluted distributions. With distributions that peaked in the 1.5 μm range, however, the eluted distributions were narrower and shifted to a smaller particle size than predicted by CFT. Apparent sticking coefficients depended on column length and flow rate, and the profile of retained iron in the columns did not follow the log-linear form expected from CFT. These observations could be rationalized in terms of the secondary energy minimum model recently proposed by Tufenkji and Elimelech (*Langmuir* **2005**, *21*, 841). For microiron, sticking coefficients correlated well with particle zeta potentials and polyacrylate (PAA) concentration. With nanoscale iron particles, there was no apparent correlation between filtration length and total electrolyte concentration. However, mixtures of PAA with poly(4-styrenesulfonate) and bentonite clay significantly enhanced nanoiron transport, possibly by affecting the aggregation of the particles.

Introduction

Industrial and agricultural processes have created contaminated soil and groundwater sites that contain dense nonaqueous phase liquids (DNAPLs), metal ions such as Cr(VI), and other persistent hazardous compounds. DNAPLs, as hydrophobic contaminants, exist in the subsurface environment in a variety of forms, including liquid ganglia and adsorbed phases in pores that equilibrate very slowly with the groundwater (*1,2*). In these cases, pump-and-treat remediation methods have had limited effectiveness, and in situ remediation technologies, in particular chemical oxidation and reduction, are now being intensively studied (*3*). Among the available reductants, zerovalent iron has been shown to be particularly effective and versatile, transforming halogenated hydrocarbons such as trichloroethylene (TCE), as well as a range of toxic metal ions, into less toxic or mobile substances (*4−10*). Because these reactions occur at the surface of iron particles, larger particles (e.g., iron filings) have lower reactivity than smaller, higher surface area iron particles. For this reason, an increasing number of laboratory and field studies of in situ remediation have been carried out using iron nano and microparticles (*11-20*).

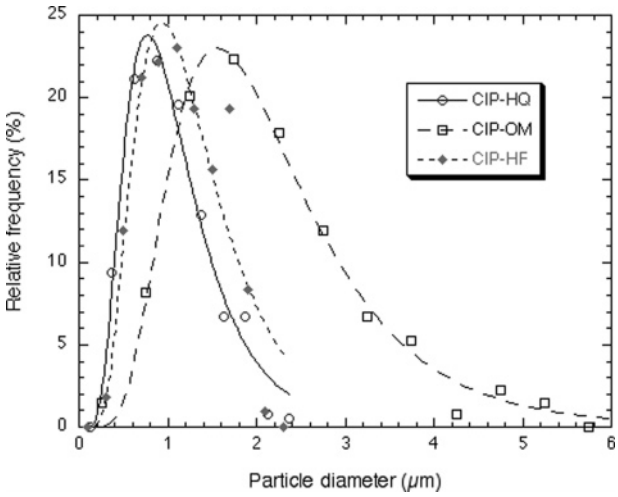

FIGURE 1. Particle diameter distributions for CIP samples. Lines represent fits to eq 1.

Delivering zerovalent iron particles to contamination sources in soil and groundwater is an interesting challenge for in situ remediation. The particles are typically injected as an aqueous slurry (*14*, *16*, *19*), and they must travel distances of meters through soil or aquifers to reach the contamination source zones. Although nanoparticles have higher reactivity with DNAPLs and metal ions, their transport properties are poorer than those of microparticles. Particles below about 200 nm in diameter undergo collisions with soil grains much more frequently than larger particles because they are subject to Brownian motion (*21*). Also, at a given mass concentration, the number density of nanoparticles is orders of magnitude higher than that of microparticles; therefore, and they are subject to aggregation. Large aggregates of nanoparticles are readily filtered and cause clogging of pores in soils (*22*).

Several strategies have been studied for improving the transport properties of iron nano- and microparticles in soils. Cantrell and co-workers used shear-thinning polymer additives to alter the fluid viscosity in soil pores and thereby decrease the frequency with which iron microparticles collide with soil grains (*23*). More recently, several groups have studied hydrophilic polymers and anionic carbons as coatings for iron nanoparticles (*24-27*). Oil-based microemulsions also stabilize nanoparticle suspensions and enhance their transport in saturated soil (*28*).

The transport of particles in the subsurface is often studied and modeled by using data from laboratory column tests. Quantitatively, one expects particles to travel over greater distances in the field, where the dispersion pathways are three-dimensional and involve a hierarchy of pore sizes (*29*). Bench-scale column tests can nevertheless provide a ranking of the effectiveness of different delivery vehicles, as well as useful kinetic information about particle filtration. One of the difficulties in modeling and optimizing the transport of iron nano- and microparticles in column tests, however, is the heterogeneity of both the particles and the collector (soil) grains. Clean-bed filtration models typically consider a

* Corresponding author phone: 814-863-9637; fax 814-863-8403; e-mail: tom@chem.psu.edu.

10.1021/es0704075 CCC: $37.00
Published on Web 08/17/2007

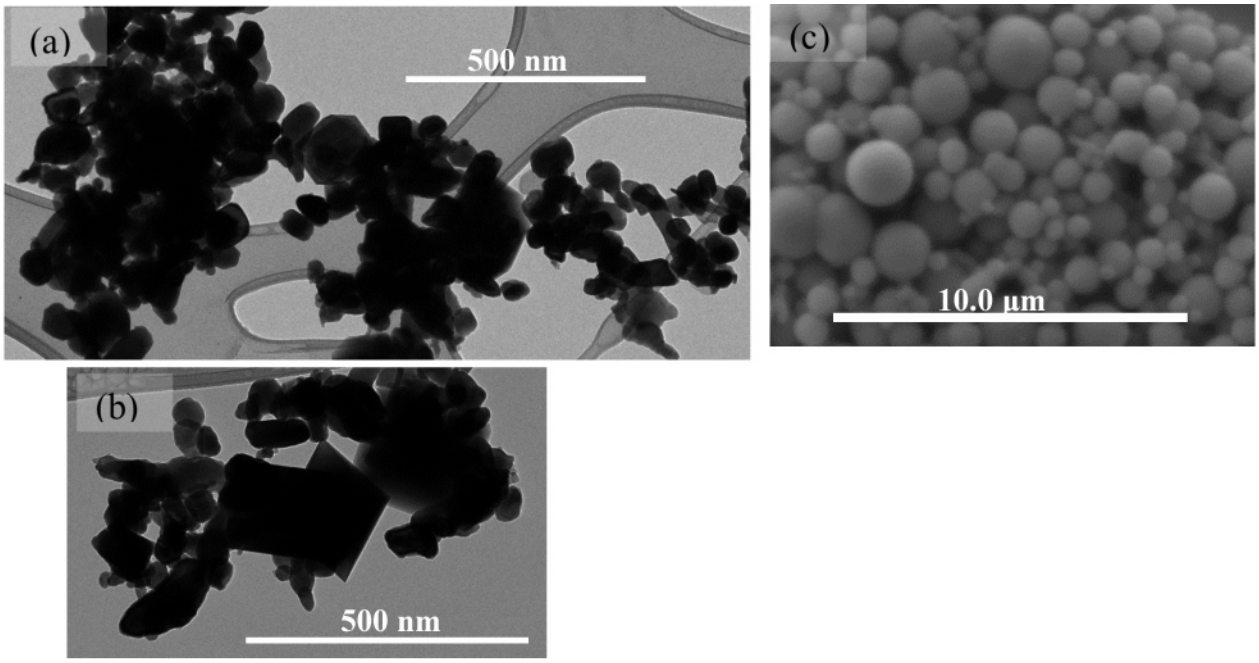

FIGURE 2. Nano- and microiron samples. (a), (b) TEM images of Toda RNIP, and (c) SEM image of CIP-HQ.

uniform collector and particle size, and model the interaction between them to obtain a single kinetic parameter, the sticking coefficient (α) (*30*, *31*). A more sophisticated filtration model recently developed by Tufenkji and Elimelech considers a range of particle-collector interaction energies (*32*). So far, this model has been tested with uniform polystyrene particles, but not with more heterogeneous samples that resemble the broad distributions used in field studies of micro- and nanoiron transport and remediation.

The goals of this study were (1) to examine the transport of polymer-coated micro- and nanoiron particles in model saturated porous media, (2) to compare the results to the predictions of current transport theories, and (3) to use this information to optimize the composition of polyelectrolyte mixtures for enhanced particle transport. Using iron microparticles in sand packed columns, we compare the predictions of first-order kinetic models with the profile of retained particles in the columns and the size distributions of the eluted particles. We also compare the qualitative features of the retention profile and eluted size distribution with a new model that considers a range of rate constants for particle collection (*32*). These comparisons provide new insight, for environmentally relevant distributions of iron particle sizes into the relative importance of particle zeta potential in the transport process. We also carried out a factorial optimization of polyelectrolyte-modified iron nanoparticle (Toda RNIP) elution from sand columns, and contrast the transport behavior of RNIP with microiron.

Results and Discussion

Particle Size Distributions. Figure 1 shows the diameter distributions of carbonyl iron powder (CIP) samples BASF CIP-HQ, -HF, and -OM, and Figure 2 shows electron micrographs of Toda Reactive Nanoiron Powder (RNIP) and CIP-HQ. Images similar to that shown in Figure 2c were obtained for CIP-HF and OM. The CIP particles have a range of diameters. The diameter (d_p) distributions for these particles were fitted to log-normal distributions (eq 1), and the best fits are shown in Figure 1. The maxima in these diameter distributions were similar for HQ and HF (0.77 and 0.93 μm, respectively), but larger for OM (1.56 μm). Within the limit of detection by X-ray powder diffraction, all three CIP samples consisted of pure α-Fe and did not contain

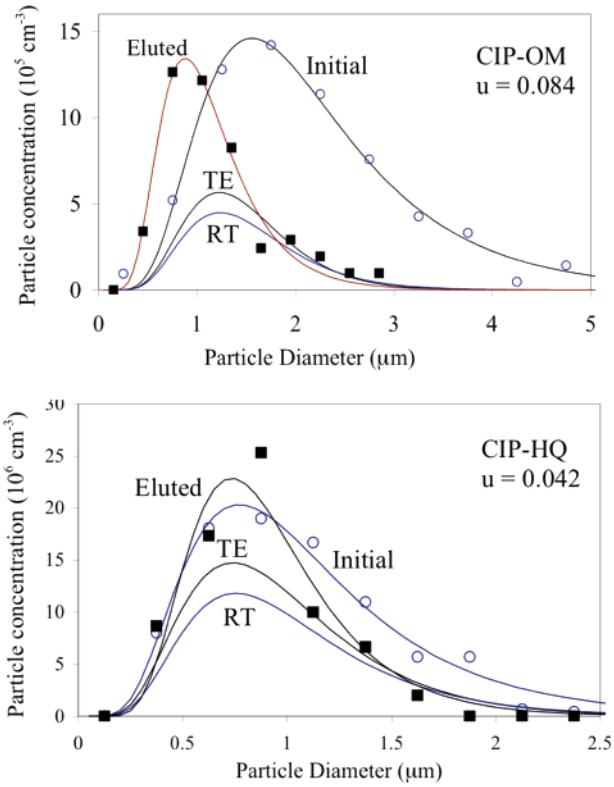

FIGURE 3. Initial (○) and eluted (■) particle size distributions for CIP-OM and CIP-HQ elution. Best fits to eq 1 are shown. Lower traces in each plot are the calculated eluted distributions from classical filtration theory, using the RT and TE models, eqs 5 and 6. Mass normalization was used to scale the eluted distributions.

significant amounts of oxide (see the Supporting Information). The RNIP particles, in contrast, were irregularly shaped and had average dimensions of 50−100 nm. Larger cubic particles with well-defined faces were

$$P(d_p) = \frac{1}{d_p \sigma \sqrt{2\pi}} \exp(-[\ln d_p - \mu]^2/2\sigma^2) \qquad (1)$$

TABLE 1. Experimental and Calculated $d_{p,max}$ Values and Calculated Sticking Coefficients; Column Length: 51.7 cm, [PAA] = 1.0 mg/mL.

CIP	flow rate (cm/s)	fraction eluted	experimental $d_{p,max}$ (μm) initial	experimental $d_{p,max}$ (μm) eluted	TE model α	TE model $d_{p,max}$ (μm)	RT model α	RT model $d_{p,max}$ (μm)
HQ	0.152	0.88	0.77	0.88	0.004	0.78	0.002	0.78
HQ	0.042	0.33	0.77	0.73	0.021	0.74	0.024	0.75
HF	0.152	0.57	0.93	0.93	0.019	0.90	0.009	0.90
HF	0.042	0.34	0.93	0.73	0.017	0.88	0.020	0.90
OM	0.152	0.20	1.56	0.88	0.033	1.37	0.017	1.36
OM	0.084	0.047	1.56	0.88	0.057	1.22	0.041	1.25

observed in some images (Figure 2b). X-ray powder diffraction patterns (see the Supporting Information) showed the presence of a significant quantity of magnetite (Fe_3O_4) in these samples in addition to α-Fe, and the larger particles in the TEM images of RNIP are believed to be magnetite.

Micro-Iron Particle Transport. CIP iron particles were dispersed in aqueous PAA solutions, and their transport through sand columns was measured by analyzing both the eluted and retained fractions. In these experiments, we sought to mimic the conditions of iron particle injection in field tests (*16*) and full-scale remediation projects (*19*). In those applications, the particles are typically pressure-injected or gravity fed into the soil as 1−10 g/L aqueous suspensions, and in many cases, the injection is followed by additional surface water and/or recirculated groundwater. In our experiments, a 2.0 mL plug of iron suspension (5.0 ± 0.5 g/L) was introduced at the top of the column and was followed by 200 mL water (approximately five pore volumes) to quantitatively elute unretained particles. The diameter distribution of the eluted particles was measured by SEM, and in the case of CIP-HQ, the amount of retained iron was analyzed as a function of column length. When the sum of the eluted and retained fractions was background corrected (by analyzing eluted blanks that contained only PAA and no iron), mass balance results were typically accurate to 10−15% (see the Supporting Information).

For each kind of CIP iron, eluted particle size distributions were measured at three different flow rates (5, 10, and 18 mL/min, = 0.042, 0.084, and 0.152 cm/s). Figure 3 shows representative results for larger (CIP-OM) and smaller diameter (CIP-HQ) initial distributions.

In all cases, the distribution of eluted particle diameters could be approximated well by eq 1. The eluted particle size distributions were normalized by constraining the mass of eluted iron to match the mass-weighted integral of the log-normal distribution. This normalization procedure is however very sensitive to counting errors at the high end of the distributions because the particle mass is proportional to the third power of the diameter. In some cases, this procedure gave the physically reasonable result that the eluted distributions contained fewer particles of every size than the initial distribution. In other cases, (see, e.g., Figure 3), the calculated maximum in the eluted distribution exceeded the number of particles of the same size in the initial distribution. While the scale factors for these fits are, therefore, uncertain, the maxima in the eluted distributions were more accurate and were consistent between duplicate runs.

Figure 3 also shows fits of the eluted quantity of iron to classical filtration theory (CFT). In CFT, which is essentially a first-order kinetic model for particle collection, the number density of particles in the mobile phase at the end of a column at length L is given by eq 2, where

$$\ln\left(\frac{N}{N_0}\right) = -\alpha\lambda L \tag{2}$$

the product $(\alpha\lambda)^{-1}$ is a filtration length (*21*). The sticking coefficient α is the probability that a particle-collector collision results in immobilization. In the "clean bed" limit, in which adsorbed particles do not cover an appreciable fraction of the surface of the porous medium, λ is obtained from eq 3, in which η is the collector efficiency, d_c is the diameter of a collector grain, and

$$\lambda = \frac{3}{2d_c}(1-\theta)\eta \tag{3}$$

θ is the soil porosity. The collector efficiency is further composed of three terms as shown in eq 4, which represent the three basic mechanisms for the capture of colloidal particles in

$$\eta = \eta_D + \eta_I + \eta_G \tag{4}$$

a packed bed: diffusion (η_D), which dominates for particles below 200 nm in diameter, interception (η_I), and gravitational sedimentation (η_G), which dominates for larger particles and aggregates of particles. Two models have been widely used to calculate these η values from experimental parameters and thereby obtain the sticking coefficient α from the fraction of particles eluted. The Rajagopalan−Tien (or RT) model (*30*) does not include hydrodynamic and universal van der Waals interactions which are included in the more recent model of Tufenkji and Elimelech (TE) (*31*). We calculated eluted particle distributions for CIP suspensions using both models (see the Supporting Information for details) to compare the results with experiment. In these calculations, the appropriate form of eq 4 was used (for the TE or RT model), and eqs 2 and 3 were used to calculate N/N_0 as a function of iron particle size. The value of α was adjusted so that the calculated mass of iron eluted (integrated over all particle sizes) matched the observed amount.

Figure 3 shows calculations of the eluted CIP particle distributions according to the RT and TE models. The data for all CIP samples, along with α values derived from the RT and TE models, are compiled in Table 1. An important parameter to compare in this table is $d_{p,max}$, the particle diameter at the maximum in the distributions. Because the experimental and calculated $d_{p,max}$ values are not sensitive to mass normalization, they provide a useful way to compare the eluted particle size distribution to the CFT calculations.

As expected for all three CIP samples, the fraction eluted increases with increasing flow rate. However, two deviations from the predictions of CFT are apparent in the data. First, the derived α values are generally lower (for a given sample) at the higher flow rate, i.e., at a higher fraction of eluted particles. Second, the experimental $d_{p,max}$ is in the range 0.73−0.93 μm for all eluted samples and the range is narrower (0.73−0.88 μm) at lower flow rates. In contrast, for CIP-OM, which initially contains larger particles, CFT predicts a significantly larger value of $d_{p,max}$ (1.22−1.37 μm). It is also apparent from Figure 3 that the eluted particle diameter distributions predicted by the CFT models are both broader than the observed distribution for CIP-OM.

Further insight into the deviation from CFT may be obtained by examining the fraction of retained iron as a function of column length. With a single particle diameter, d_p, CFT predicts an exponential profile of retained particles according to eq 2. However, with a distribution of particle sizes, the situation is more complex. Because the largest and smallest particles in the distribution are filtered more efficiently, the average filtration length $(\alpha\lambda)^{-1}$ increases slightly with increasing

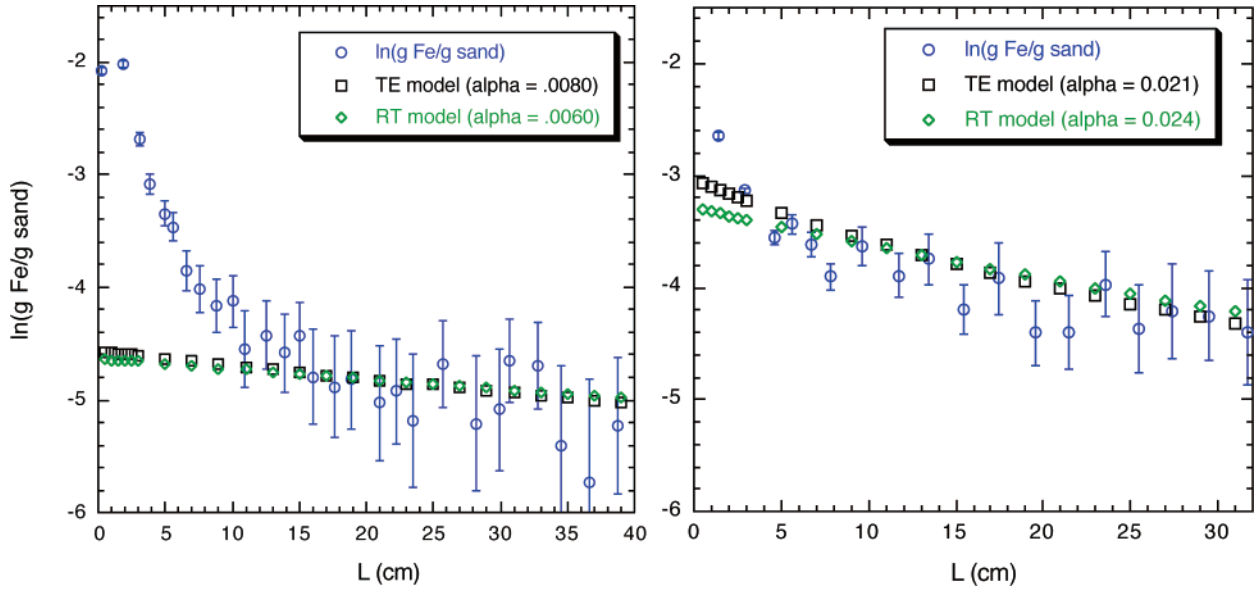

FIGURE 4. Natural logarithm of the experimental and calculated retained iron profiles for CIP-HQ/1 mg/mL PAA. Left: Darcy velocity *u* = 0.084 cm/s; right: *u* = 0.042 cm/s.

column length L. Rewriting eq 2 in exponential form, we obtain eq 5.

$$\frac{N}{N_0} = e^{-\alpha\lambda L} \tag{5}$$

For a distribution of particles, this must be rewritten as eq 6, which is a sum over all values

$$\mathrm{N}(L) = \sum_{d_\mathrm{p}} \mathrm{N}_0(d_\mathrm{p}) e^{-\alpha\lambda(d_p)L} \tag{6}$$

of particle diameter d_p. The number density of particles N (particles/cm^3) can be converted to the mass concentration of iron in the mobile phase, M(L) (mass/cm^3), by using eq 7, where V is the particle volume ($V = 4/3\ \pi r^3$) and ρ is the specific gravity of iron.

$$\mathrm{M(L)} = \rho \sum_{d_\mathrm{p}} \mathrm{N}_0(d_\mathrm{p}) V(d_\mathrm{p}) e^{-\alpha\lambda(d_p)L} \tag{7}$$

Finally, the retained fraction (mass of iron retained per unit length) can be calculated from the gradient of M(L) according to eq 8, where θ is the column porosity and A is the cross-sectional area.

$$\frac{d\mathrm{M}_{\mathrm{retained}}(\mathrm{L})}{d\mathrm{L}} = -\frac{d\mathrm{M(L)}}{d\mathrm{L}} \times \theta \times A \tag{8}$$

Figure 4 compares the experimental retained mass distribution of CIP-HQ iron with the distributions calculated from eqs 7 and 8 using α values obtained from the TE and RT models. The distribution of particle sizes introduces a slight upward curvature into the calculated retained profile. However, the experimental profiles are much more sharply curved. This behavior is consistent with the more recent model of Tufenkji and Elimelech which considers a range of particle-collector interaction energies and rate constants (*32*). In this model, larger particles are collected at a faster rate because they are trapped by van der Waals forces in a secondary energy minimum that is deep relative to the thermal energy. Very similar curvature in retained profiles was seen in their experiments with latex particles and columns of glass collectors. This effect is consistent with several observations in our data: the sharpening of eluted particle size distributions (Figure 3), the shift to $d_{\mathrm{p,max}}$ values smaller than expected from CFT (Table 1), the increase in apparent α values with decreasing flow rate (Table 1), and the decrease in apparent α values with increasing column length (see Figure 5 below). If particle elution data (Table 1) are fit to a single value of α using one of the CFT models, the nonexponential profile of retained iron (Figure 4) implies that longer columns should give smaller "average" α values.

Effect of PAA Concentration on the Transport of Microiron Particles. To gain insight into the effect of added PAA on the sticking coefficient (α), the concentration of PAA in the stock CIP iron suspensions was varied between 0.5 and 5.0 mg/mL. Sticking coefficients were calculated from the fraction of iron eluted using the TE model, and the results are shown in Figure 5. These results are compared with zeta potential measurements of the same particles over a broader range of PAA concentrations (0−100 mg/mL).

The addition of PAA to the suspensions imparts substantial negative charge to the particles, most likely by chelation of the polyacid to the iron oxide or hydroxide at the particle surface (*24*). In pure water, the measured ζ values were −15, −19, and −20 ± 2 mV for CIP-HQ, OM, and HF, respectively. At the PAA concentrations used in the sand column experiments, ζ values were in the range of −60 to −90 mV. The primary effect of the large negative charge on the particle surface is to cause electrostatic repulsion between the particles and the negatively charged collector grains. For CIP-HF, α decreases substantially as the PAA concentration is increased from 1 to 5 mg/mL, and there is also a significant change in the zeta potential. For CIP-HQ, the changes in both quantities are more gradual. There is apparently a subtle difference in the surface chemistry of these otherwise very similar particles. CIP-HQ particles retain their negative charge after exposure to concentrated PAA solutions (1000 mg/mL) and rinsing with deionized water (ζ = −61), but with the same treatment ζ = −28 and −32 mV for CIP-OM and HF, respectively. At the concentrations of PAA used in the transport experiments, there is a very large excess of polymer relative to the number of surface sites on the low surface area microiron particles. It is therefore possible that other effects of the excess polyelectrolyte, such as blocking of strong adsorption sites on the collector grains (*33*) or macromolecular crowding (*34*), contribute to the decrease in α with increasing PAA concentration. However, these effects should not lead to differences in α values for CIP-HQ and CIP-HF,

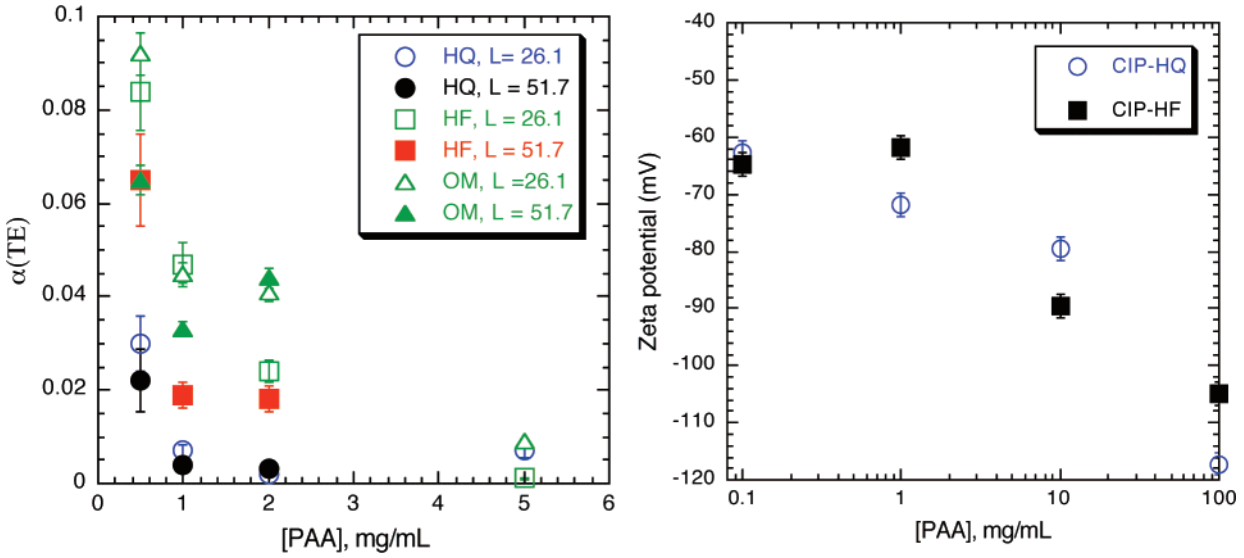

FIGURE 5. Left: Sticking coefficient, α(TE) vs PAA concentration for CIP-HQ, HF, and OM elution from 26.1 cm (open plot symbols) and 51.7 cm (solid plot symbols) columns. Flow rate = 0.151 cm/s. Right: ζ vs PAA concentration for CIP-HQ and HF.

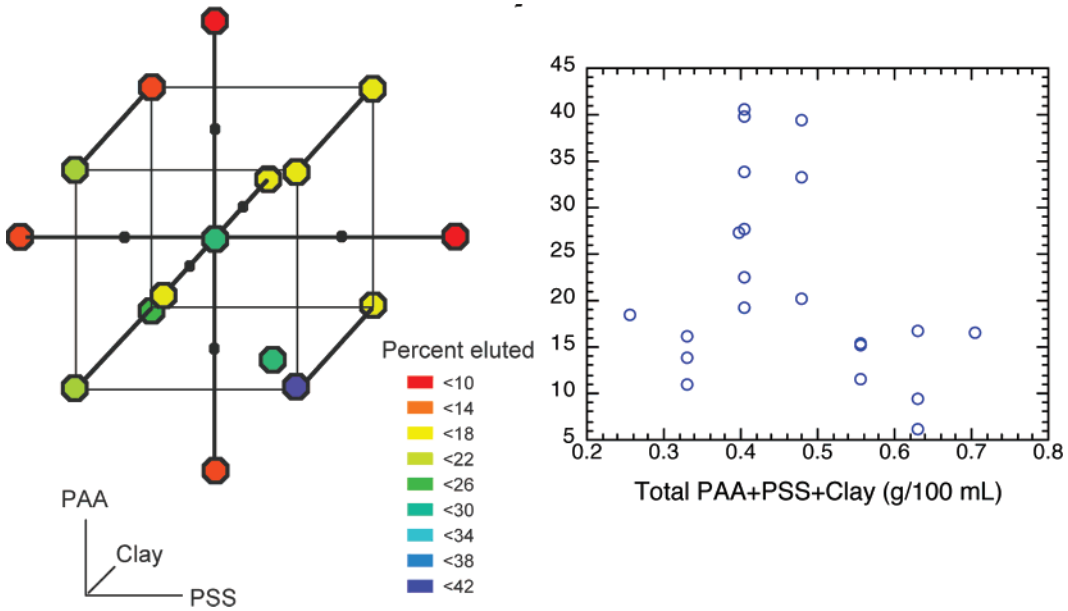

FIGURE 6. Left: Three factor orthogonal central composite design (CCD) (*35*), showing percent of RNIP eluted. Each circle represents a mixture of polyelectrolytes with a high, middle, or low concentration of one component, and the center point represents an average value of all three concentrations. The eight factorial points at the corners of the cube represent mixtures with intermediate concentration values. Right: Scatter plot of percent elution vs total polyelectrolyte composition. Column length (71 cm), flow rate (18 mL/min), and RNIP concentration (10 mg/mL) were held constant.

which are quite significant at PAA concentrations of 1−2 mg/mL. The dominant effect of increasing polyanion concentration is therefore to increase the negative surface charge of the microiron particles.

Effect of Polyelectrolytes on the Transport of Nanoiron Suspensions. The transport of nanoiron is more complex than that of microiron, primarily because of the tendency of nanoparticles to aggregate and the strong dependence of $(\alpha\lambda)^{-1}$ on particle size in the nanoscale regime. Saleh et al. have recently studied RNIP modified with anionic block copolymers and found that particle zeta potential does not correlate directly with filtration length (*27*). The dependence of eluted fraction on particle concentration that they observed also suggests that aggregation plays a role, and that aggregate straining rather than filtration is an important component of particle capture. These factors complicate the problem of developing and testing a quantitative model for RNIP transport. Despite this problem, it is important to optimize the transport of iron nanoparticles because they have the most utility for in situ remediation.

In our earlier study, we found that PAA enhanced nanoparticle transport, and was especially effective in a clay-rich soil (*24*). This result seems counterintuitive, given the fine texture of clay soils and the strong dependence of filtration length on collector diameter. It is important to recall, however, that swelling clays are also anionic polyelectrolytes and may thus affect particle zeta potential or block strong adsorption sites on other collector surfaces. To explore these effects, we conducted RNIP transport studies with mixtures of polyelectrolytes: PAA, a low molecular weight coordinating polyanion, poly(sodium 4-styrenesulfonate) (PSS), a high molecular weight, noncoordinating polyanion, and bentonite clay. Fifteen different electrolyte mixtures were chosen, based on a three-parameter central composite design (CCD)

factorial array, as illustrated in Figure 6.

The fraction of RNIP eluted in these experiments depended sensitively on the composition of the electrolyte mixture. With 71 cm sand columns, this fraction ranged between 6 and 40%, with the highest elution fraction at relatively high PSS concentration (2.5 mg/mL) and lower concentrations of PAA and clay (1.0 and 0.8 mg/mL, respectively). Surprisingly, there was no apparent trend with total poly(anion) concentration, contrary to the results obtained with microiron (see Figure 5). This suggests that the most important effects of the other added electrolytes may be to control particle aggregation or other factors, rather than simply to change the zeta potential and thereby affect the particle-collector interaction potential. Ditsch et al., using similar mixtures of PAA, PSS, and copolymers, have shown that aggregation of oxide nanoparticles can be controlled by properly controlling the molecular weight and order of addition of the components (*36*). Recently, Lowry and coworkers have quantified the aggregation of unmodified RNIP particles as a function of particle concentration and time (*37*). Given the strong sensitivity of the filtration length to particle (or aggregate) size in the nanoscale regime, this can clearly be an important parameter in the transport of RNIP.

The transport behavior of RNIP nanoiron suspensions is qualitatively different from that of CIP suspensions in that there was no clear correlation between filtration length and total electrolyte concentration. These trends appear to merit further study, particularly in understanding the role of clays and polymeric electrolytes in controlling nanoparticle aggregation. Phenomenologically, we have observed that the filtration length of RNIP is sensitive to the composition of the polyelectrolyte suspension. With ternary mixtures containing PAA, PSS, and bentonite clay, the filtration length can be extended by a factor of 3−4 relative to polyacrylate alone. This finding may have useful consequences for remediation studies like that described in ref *19*, in which iron nanoparticles must travel distances of meters through saturated soils to reach contaminant source zones.

Acknowledgments

This work was supported by the National Science Foundation under grant CHE-0616450. We thank Adrian Goodey for help in obtaining SEM images, Rafaat Malek for use of the ZetaPALS instrument, Kaiti Liao, Kiran Gill, and Christopher Nelson (PARS Environmental) for assisting in preliminary RNIP transport experiments, and Mark Torgerson (BASF), Harch Gill (PARS Environmental), Andy Jazdinian (Toda America) and Kenji Okinaka (Toda Kogyo) for contributing materials used in this study. Finally, we thank Bruce Logan for many helpful discussions about particle filtration and environmental transport processes.

Supporting Information Available

Materials and detailed experimental procedures for column transport experiments, and parameters used in transport simulations are described. This materials is available free of charge via the Internet at http://pubs.acs.org.

Literature Cited

(1) Luthy, R. G.; Aiken, G. R.; Brusseau, M. L.; Cunningham, S. D.; Gschwend, P. M.; Pignatello, J. J.; Reinhard, M.; Traina, S. J.; Weber, W. J., Jr.; Westall, J. C. Sequestration of hydrophobic organic contaminants by geosorbents, *Environ. Sci. Technol.* **1997**, *31*, 3341−3347.

(2) Zhang, W.; Bouwer, E.; Ball, W. Bioavailability of hydrophobic organic contaminants: effects and implications of sorption-related mass transfer on bioremediation, *Ground Water Monit. Rem.* **1998**, *18* (1), pp. 126−138.

(3) *Contaminants in the Subsurface: Source Zone Assessment and Remediation*; Water Science and Technology Board, National Research Council of the National Academies. National Academies Press: Washington, DC, 2004; pp 194−217.

(4) Gillham, R. W.; O'Hannesin, S. F. Enhanced degradation of halogenated aliphatics by zero-valent iron. *Ground Water* **1994**, *32*, 958−967.

(5) Matheson, L. J.; Tratnyek, P. G. Reductive dehalogenation of chlorinated methanes by iron metal. *Environ. Sci. Technol.* **1994**, *28*, 2045−2053.

(6) Roberts, A. L.; Totten, L. A.; Arnold, W. A.; Burris, D. R.; Campbell, T. J. Reductive elimination of chlorinated ethylenes by zero-valent metals. *Environ. Sci. Technol.* **1996**, *30*, 2654−2659.

(7) Tratnyek, P. G.; Johnson, T. L.; Scherer, M. M.; Eykholt, G. R. Remediating ground water with zero-valent metals: Chemical considerations in barrier design. *Ground Water Monit. Rem.* **1997**, *17* (4), 108−114.

(8) Liang, L.; Korte, N.; Goodlaxson, J. D.; Clausen, J.; Fernando, Q.; Muftikian, R. Byproduct formation during the reduction of TCE by zero-valence iron and palladized iron. *Ground Water Monit. Rem.* **1997**, *17* (1), 122−127.

(9) Blowes, D. W.; Ptacek, C. J.; Jambor, J. L. In-situ remediation of Cr(VI)-contaminated groundwater using permeable reactive walls: laboratory studies. *Environ. Sci. Technol.* **1997**, *31*, 3348−3357.

(10) Powell, R. M.; Puls, R. W.; Hightower, S. K.; Sabatini, D. A. Coupled iron corrosion and chromate reduction: Mechanisms for subsurface remediation *Environ. Sci. Technol.* **1995**, *29*, 1913−1922.

(11) Zhang, W. X. Nanoscale iron particles for environmental remediation: an overview. *J. Nanopart. Res.* **2003**, *5*, 323−332.

(12) Boronina, T.; Klabunde, K. J.; Sergeev, G. Destruction of organohalides in water using metal particles: carbon tetrachloride/water reactions with magnesium, tin, and zinc. *Environ. Sci. Technol.* **1995**, *29*, 1511−1517.

(13) Wang, C.-B.; Zhang, W.-X. Synthesizing nanoscale iron particles for rapid and complete dechlorination of TCE and PCBs. *Environ. Sci. Technol.* **1997**, *31* (7), 2154−2156.

(14) Kaplan, D. I.; Cantrell, K. J.; Wietsma, T. J.; Potter, M. A. Retention of zero-valent iron colloids by sand columns: application to chemical barrier formation. *J. Environ. Qual.* **1996**, *25*, 1086−1094.

(15) Ponder, S. M.; Darab, J. G.; Mallouk, T. E. Remediation of Cr(VI) and Pb(II) aqueous solutions using supported, nanoscale zero-valent iron. *Environ. Sci. Technol.* **2000**, *34*, 2564−2569.

(16) Elliott, D. W.; Zhang, W.-X. Field assessment of nanoscale bimetallic particles for groundwater treatment. *Environ. Sci. Technol.* **2001**, *35*, 4922−4926.

(17) Schrick, B.; Blough, J. L.; Jones, A. D.; Mallouk, T. E. Hydrodechlorination of trichloroethylene to hydrocarbons using bimetallic nickel-iron nanoparticles. *Chem. Mater.* **2002**, *14*, 5140−5147.

(18) Liu, Y. Q.; Majetich, S. A.; Tilton, R. D.; Sholl, D. S.; Lowry, G. V. TCE dechlorination rates, pathways, and efficiency of nanoscale iron particles with different properties. *Environ. Sci. Technol.* **2005**, *39*, 1338−1345.

(19) Varadhi, S. N.; Gill, H. S.; Apoldo, L. J.; Liao, K.; Blackman, R. A.; Wittman, W. K. Full-Scale Nanoiron Injection for Treatment of Groundwater Contaminated with Chlorinated Hydrocarbons, Natural Gas Technologies,February, 2005, Orlando, FL, 2005.

(20) Kanel, S. R.; Choi, H. The transport characteristics of polymer stabilized nano scale zero-valent iron in porous media. *Water Sci. Technol.* **2007**, *55*, 157−162.

(21) Yao, K.-M.; Habibian, M. T.; O'Melia, C. R. Water and waste water filtration. Concepts and applications. *Environ. Sci. Technol.* **1971**, *5*, 1105−1112.

(22) Logan, B. E., *Environmental Transport Processes*; John Wiley and Sons: New York, 1999; pp 564−613.

(23) Cantrell, K. J.; Kaplan, D. I.; Gilmore, T. J. Injection of colloidal Fe^0 particles in sand with shear-thinning fluids. *J. Environ. Eng.* **1997**, *123*, 786−791.

(24) Schrick, B.; Hydutsky, B. W.; Blough, J. L.; Mallouk, T. E. Delivery vehicles for zerovalent metal nanoparticles in soil and groundwater. *Chem. Mater.* **2004**, *16*, 2187−2193.

(25) He, F.; Zhao, D. Preparation and characterization of a new class of starch-stabilized bimetallic nanoparticles for degradation of chlorinated hydrocarbons in water. *Environ. Sci. Technol.* **2005**, *39*, 3314−3320.

(26) Saleh, N.; Phenrat, T.; Sirk, K.; Dufour, B.; Ok, J.; Sarbu, T.; Matyjaszewski, K.; Tilton, R. D.; Lowry, G. V. Adsorbed triblock copolymers deliver reactive iron nanoparticles to the oil/water interface. *Nano Lett.* **2005**, *5*, 2489.

(27) Saleh, N.; Sirk, K.; Liu, Y.; Phenrat, T.; Dufour, B.; Matyjaszeski, K.; Tilton, R. D.; Lowry, G. V. Surface modifications enhance

nanoiron transport and NAPL targeting in saturated porous media. *Environ. Eng. Sci.* **2007**, *24*, 45−57.
(28) Quinn, J.; Geiger, C.; Clausen, C.; Brooks, K.; Coon, C.; O'Hara, S.; Krug, T.; Major, D.; Yoon, W.-S.; Gavaskar, A.; Holdsworth, T. Field demonstration of DNAPL dehalogenation using emulsified zero-valent iron. *Environ. Sci. Technol.* **2005**, *39*, 1309−1318.
(29) Gelhar, L. W. C.; Welty, C.; Rehfeldt, K. R. Critical review of data on field-scale dispersion in aquifers. *Water Resour. Res.* **1992**, *28*, 1955−1974.
(30) Rajagopalan, R.; Tien, C. Trajectory analysis of deep-bed filtration with the sphere-in-cell porous media model. *AIChE J.* **1976**, *22*, 523−533.
(31) Tufenkji, N.; Elimelech, M. Correlation equation for predicting single-collector efficiency in physicochemical filtration in saturated porous media. *Environ. Sci. Technol.* **2004**, *38*, 529−539.
(32) Tufenkji, N.; Elimelech, M. Breakdown of colloid filtration theory: role of the secondary energy minimum and surface charge heterogeneities. *Langmuir* **2005**, *21*, 841−852.
(33) Ryan, J. N.; Elimelech, M. Colloid immobilization and transport in groundwater. *Colloids Surf. A* **1996**, *107*, 1−56.
(34) Tohver, V.; Smay, J. E.; Braem, A.; Braun, P. V.; Lewis, J. A. Nanoparticle halos: A new colloid stabilization mechanism. *Proc. Nat. Acad. Sci. U. S. A.* **2001**, *98*, 8950−8954.
(35) Langhans, I. Designs for response surface modeling − quantifying the relation between factors and response. In *Design and Analysis in Chemical Research*; Tranter, R. L., Ed.; CRC Press: Boca Raton, FL, 2000; pp 237−278.
(36) Ditsch, A.; Laibinis, P. E.; Wang, D. I. C.; Hatton, T. A. Controlled clustering and enhanced stability of polymer-coated magnetic nanoparticles. *Langmuir* **2005**, *21*, 6006−6018.
(37) Phenrat, T.; Saleh, N.; Sirk, K.; Tilton, R. D.; Lowry, G. V. Aggregation and sedimentation of aqueous nanoscale zerovalent iron dispersions. *Environ. Sci. Technol.* **2007**, *41*, 284−290.

Received for review February 16, 2007. Revised manuscript received July 1, 2007. Accepted July 2, 2007.

ES0704075